DOI: 10.1002/((please add manuscript number))
Article type: Communication

Exploring Bi_2Te_3 nanoplates as versatile catalysts for electrochemical reduction of small molecules

Nan Zhang[+], Fangfang Zheng[+], Bolong Huang[+], Yujin Ji, Qi Shao, Youyong Li, Xiangheng Xiao, Xiaoqing Huang[*]

N. Zhang, Dr. Q. Shao, Prof. X. Huang
College of Chemistry, Chemical Engineering and Materials Science, Soochow University, Jiangsu 215123, China
E-mail: hxq006@suda.edu.cn
N. Zhang, Prof. X. Xiao
School of Physics and Technology, Wuhan University, Hubei 430072, China
F. Zheng, Y. Ji, Prof. Y. Li
Institute of Functional Nano & Soft Materials (FUNSOM), Jiangsu Key Laboratory for Carbon-Based Functional Materials & Devices, Soochow University, Suzhou, Jiangsu 215123, China
Prof. B. Huang
Department of Applied Biology and Chemical Technology, The Hong Kong Polytechnic University, Hung Hom, Kowloon, Hong Kong SAR, China

Abstract: The electroreduction of small molecules to high value-added chemicals is considered as a promising way to the capture and utilization of atmospheric small molecules, such as O_2, CO_2 and N_2. Discovering cheap and efficient electrocatalysts with simultaneously high activity, selectivity, durability and even universality is particularly desirable yet challenging. Herein, we first demonstrate that ultrathin Bi_2Te_3 nanoplates (NPs), cheap and noble metal-free electrocatalysts, can be adopted as highly universal and robust electrocatalysts, which can efficiently realize the reduction of small molecules (O_2, CO_2 and N_2) into targeted products simultaneously. They can achieve high activity and selectivity, as

well as excellent durability of O_2 reduction reaction with almost 100% H_2O_2 selectivity, CO_2 reduction reaction with up to 90% Faradaic efficiency (FE) of HCOOH as well as N_2 reduction reaction with 7.9% FE of NH_3. We found that, after electrochemical activation, an obvious Te dissolution happened on the Bi_2Te_3 NPs, which is the key to the creation of a large amount of Te vacancies in the activated Bi_2Te_3 NPs. Theoretical calculations revealed that the Te vacancies on the Bi_2Te_3 surface enable the modulation of the electronic structures of Bi and Te. The Bi and Te are playing the opposite role, in which Bi-6p atoms are the electron suppliers while the Te atoms the electronic depletion center, respectively. Such a highly electroactive surface with a strong preference in supplying electrons for the universal reduction reactions to improve the electrocatalytic performance of Bi_2Te_3. Our experiments and theoretical work demonstrated a new class of cheap and versatile catalysts for the electrochemical reduction of small molecules with potential practical applications.

Keywords: Bi_2Te_3 nanoplate • Universality • Oxygen reduction reaction • Carbon dioxide reduction reaction • Nitrogen reduction reaction

In the past years, the utilization and conversion of earth-abundant, atmospheric molecules, such as O_2, CO_2 and N_2, have been received many research interests, since it is an efficient way to generate value-added chemical intermediates and fuels. While several typical industrial processes, such as Haber-Bosch process, anthraquinone process etc., are the main routes to produce the important intermediates and fuels (i. e., H_2O_2, HCOOH and NH_3), it still comes with many problems, such as extreme energy dependence, explosion dangers, environmental pollution, limited efficiency and so on.[1-3] The electrochemical approach, being milder, cleaner and more efficient, has emerged as a versatile route for yielding the important chemical intermediates and fuels *via* these electrochemical conversions.[4-8] In electrocatalysis, while the electrocatalysts play a vital role in reducing the activation energy of

the reaction and driving the reaction, developing highly efficient electrocatalysts is of great significance.

H_2O_2 is one of the 100 most important chemicals.[1] Industrially, H_2O_2 is prepared by direct oxidation of H_2, which is however with the danger of explosion.[9,10] O_2 reduction reaction (ORR) represents an attractive alternative to prepare H_2O_2 with the feature of environmentally friendly and safe, but electrocatalysts suffer from high cost, limited selectivity and/or low activity.[1,2,11,12] Besides H_2O_2, HCOOH, an important intermediate in industry and the chemical fuel in direct HCOOH fuel cells, is a common CO_2 reduction reaction (CO_2RR) product,[13-15] but developing the active, selective, durable and cheap electrocatalysts for CO_2RR is also very challenging.[16-21] NH_3, another highly value-added chemical, is one of the most widely-used chemicals because it is a source of N_2 for fertilizer and potential transportation fuel.[22-25] While N_2 reduction reaction (N_2RR) into NH_3 represents an attractive prospect for the fixation of N_2,[22, 26-30] it suffers from a low yield rate of NH_3 over reported electrocatalysts.[31,32] Based on the above considerations, although small molecules electroreduction is indeed a promising route to obtain value-added chemicals, it is still very challenging to simultaneously reach desirable activity, selectivity and cost. As the electrocatalysts are the key for those reductions, it is particularly urgent to explore low-cost, high-performance catalysts with enhanced efficiency. In particular, it would be a formidable challenge to discover universal electrocatalysts to simultaneously realize high performance for the electroreduction of various small molecules.

Herein, we first demonstrate that the ultrathin Bi_2Te_3 nanoplates (NPs) can be adopted as highly universal, cheap, active and selective noble metal-free electrocatalysts for small molecules (i. e., O_2, CO_2 and N_2) reductions. The ultrathin Bi_2Te_3 NPs could simultaneously achieve high activity and selectivity, as well as excellent durability for ORR, CO_2RR as well as N_2RR. Specifically, the Bi_2Te_3 NPs showed nearly 100% H_2O_2 selectivity for ORR, 89.6%

Faradaic efficiency (FE) of HCOOH for CO_2RR as well as 7.9% FE of NH_3 for N_2RR. After electrochemical activation, a large amount of Te vacancies were produced on the Bi_2Te_3 NPs because of the obvious Te dissolution. DFT calculations further verified the formation of Te vacancies will significantly optimize the surface electronic distribution for the electro-reduction towards small molecule reactions. The Bi_2Te_3 NPs were also stable in the reduction reactions of small molecules with negligible activity decay after the durability tests.

The ultrathin Bi-Te NPs were synthesized through a facile hydrothermal reaction with bismuth chloride ($BiCl_3$) and potassium tellurite (K_2TeO_3) as precursors, polyvinyl pyrrolidone (PVP, MW = 58000) as surfactant and ethylene glycol as the solvent in the presence of sodium hydroxide (NaOH) (see the supporting information for details). The NPs were initially characterized by high-angle annular dark-field scanning transmission electron microscopy (HAADF-STEM). The hexagonal NPs were the dominant product with a monodisperse edge length of about 450 nm (**Figure 1a**). The thickness of Bi-Te NPs was determined to be around 16.5 nm by atomic force microscope (AFM) (**Figure 1b)**. The Bi/Te molar ratio of the NPs was determined to be 2/3 by scanning electron microscopy energy-dispersive X-ray spectroscopy (SEM-EDS) (**Figure S1a**). The powder X-ray diffraction (PXRD) pattern of the products displayed distinct patterns associated with Bi_2Te_3 materials (**Figure S1b**). In addition, the high-resolution TEM (HRTEM) image of the NP (**Figure 1c**) showed the lattice fringes with an interplanar spacing of 0.222 nm, corresponding to the (110) plane of the Bi_2Te_3 materials. The Bi_2Te_3 NPs were further characterized by the line scan analysis, where the distributions of Bi and Te were throughout the whole NP (**Figure 1d**), being consistent with the HAADF-STEM-EDS elemental mapping result (**Figure 1e**).

The prepared Bi_2Te_3 NPs were then loaded on a commercial carbon (Vulcan XC72R carbon, C) *via* sonication, then thoroughly washed with ethanol for electrocatalysis (**Figure S2**). The commercial Bi_2Te_3 (**Figure S3**) was taken as reference for comparison. The

commercial Bi_2Te_3 were also loaded on a commercial carbon (**Figure S4**). The loading amount of the two catalysts was both 50 wt% based on the inductively coupled plasma atomic emission spectroscopy (ICP-AES). Before the electroreduction, the Bi_2Te_3 NPs/C was activated by cycling in 0.1 M KOH for 500 cycles. The double-layer capacitance (C_{dl}) values of the Bi_2Te_3 NPs/C and the commercial Bi_2Te_3/C were initially tested, which is positively correlated with the electrochemical active surface area (ECSA) (**Figure S5a,c**).[33,34] As shown in **Figure S5b,d**, the C_{dl} of the Bi_2Te_3 NPs/C was 16.7 mF cm^{-2}, which was much higher than that of the commercial Bi_2Te_3/C (3.8 mF cm^{-2}). Furthermore, the ECSA of the activated Bi_2Te_3 NPs/C was also measured by the Cdl values. As shown in **Figure S6**, the C_{dl} value of the activated one was 20 mF cm^{-2}, which is higher than the initial one (16.7 mF cm^{-2}). The higher C_{dl} value of the activated Bi_2Te_3 NPs/C is beneficial for enhancing the relevant electroreductions.

The activated Bi_2Te_3 NPs/C was initially evaluated as electrocatalyst for ORR. The ORR activity for Bi_2Te_3 NPs/C was tested with a rotating ring disk electrode (RRDE) setup at 1600 rpm in O_2-saturated 0.1 M KOH. The commercial Bi_2Te_3, carbon and the glassy carbon electrode (GC) were used as the references. The ring electrode was Pt and held at 1.2 V *vs.* reversible hydrogen electrode (RHE) to oxidize H_2O_2 formed on the disk electrode, allowing for ORR product quantification. The collection efficiency (N) is an important parameter to calculate the H_2O_2 selectivity. The value of N was experimentally determined to be 0.29 by using a standard ferricyanide system (**Figure S7**).[35] **Figure 2a** shows O_2 reduction disk currents and the simultaneously measured peroxide oxidation ring currents for the activated Bi_2Te_3 NPs/C, the commercial Bi_2Te_3/C, carbon and GC. The amount of H_2O_2 produced was monitored at the ring electrode, where a positive current was measured once H_2O_2 was produced at the disk. The H_2O_2 selectivity of the activated Bi_2Te_3 NPs/C reached more than 95% at a potential between 0.2 V_{RHE} and 0.6 V_{RHE} (**Figure 2b**), indicating that a high yield of

H_2O_2 was achievable. As for the commercial Bi_2Te_3/C, the H_2O_2 selectivity was only around 80% at a smaller potential range (0.2 V_{RHE} - 0.4 V_{RHE}). It should be noted that the H_2O_2 selectivity of the activated Bi_2Te_3 NPs/C is the highest in the reported materials, which is even better than many noble-metal catalysts such as Pd-Au,[11] Pt-Hg,[36] Pd-Hg,[37] Au-Pt-Ni[38] and so on (**Table S1**). Furthermore, the number of the transferred electrons (*n*) (**Figure 2c**) for the activated Bi_2Te_3 NPs/C was calculated to be around 2.0 during 0.2 V_{RHE} from 0.6 V_{RHE}, suggesting a dominant 2-electron O_2 reduction pathway. To further confirm that the ring and disk currents were produced by the reduction of O_2 based on the activated Bi_2Te_3 NPs/C, we further measured the ORR polarization curve of the activated Bi_2Te_3 NPs/C by O_2 saturation, where the electrolyte was initially saturated by Ar. The ring and disk current densities of the activated Bi_2Te_3 NPs/C were close to that in the electrolyte initially saturated by N_2, indicating that no N_2RR happens during the ORR process (**Figure S8**). The activated Bi_2Te_3 NPs/C is also durable since both the ring and disk currents can maintain over 10 h, as revealed by the potentiostatic measurement (**Figure 2d**).

We next investigated the CO_2RR performance of the activated Bi_2Te_3 NPs/C in an H-cell containing 30 mL 0.5 M $NaHCO_3$. As shown in **Figure 3a**, the activated Bi_2Te_3 NPs/C showed a remarkable enhancement of the CO_2 reduction. The polarization curve of the activated Bi_2Te_3 NPs/C in CO_2-saturated 0.5 M $NaHCO_3$ showed a cathodic current onset at around -0.7 V_{RHE}, and then its current density continued to increase. When the potential reached to -1.1 V_{RHE}, the activated Bi_2Te_3 NPs/C could reach a current density of about 31 mA cm^{-2}, significantly higher than that of the commercial Bi_2Te_3/C. The reduction reactions of Te^{2+} and Bi^{3+} caused the reduction peaks at -0.5 V_{RHE} and 0.35 V_{RHE}, respectively.[39,40] In the control experiment, the polarization curves in the Ar-saturated 0.5 M $NaHCO_3$ of the activated Bi_2Te_3 NPs/C and the commercial Bi_2Te_3/C showed that the current densities were significantly reduced. To identify and quantify the reduction products, gas chromatography

and ^{1}H NMR spectroscopy were performed to quantify the gaseous and liquid products, respectively. The product in CO_2RR included HCOOH, CO, and H_2 over the activated Bi_2Te_3 NPs/C and the commercial Bi_2Te_3/C. We found that HCOOH was the major product, along with a small amount of CO and H_2. FEs of HCOOH, CO and H_2 at various potentials were calculated and summarized in **Figure 3b and Figure S9**. We can see that the activated Bi_2Te_3 NPs/C showed more than 70% FE_{HCOOH} over a wide voltage range. When the potential was increased to -0.9 V_{RHE}, the FE_{HCOOH} reached up to 89.6% (**Figure S10**). In addition, the FE_{CO} was less than 3% at the wide range of applied potentials. The FE_{H2} underwent a significant decrease with increasing potential, where only small FE_{H2} was detected at the high potentials. For the commercial Bi_2Te_3/C, the FE_{HCOOH} reached the peak value of only 58.1% at -0.8 V_{RHE} (**Figure 3b**). Therefore, the FE_{HCOOH} for the activated Bi_2Te_3 NPs/C was higher than the most state of the art catalysts for HCOOH productions in CO_2RR (**Table S2**). The FE_{HCOOH} for the activated Bi_2Te_3 NPs/C was even comparable to the value for the partially oxidized Co layers reported in Nature.[41] Furthermore, the partial current densities of HCOOH for the different catalysts were further calculated and plotted against the working potential (**Figure 3c**). The activated Bi_2Te_3 NPs/C delivered a maximum value of j_{HCOOH} = 24.2 mA cm^{-2} at -1.1 V_{RHE}, whereas that of the latter was only 5.2 mA cm^{-2}. The activated Bi_2Te_3 NPs/C also showed enhanced durability with maintaining high FE_{HCOOH} of 88.7% after 10 h potentiostatic test at -0.9 V_{RHE} (**Figure S11**).

Inspired by the excellent performance of the activated Bi_2Te_3 NPs/C for ORR and CO_2RR, the performance of the activated Bi_2Te_3 NPs/C for N_2RR was further investigated. The polarization curves of the activated Bi_2Te_3 NPs/C and the commercial Bi_2Te_3/C in both Ar-saturated and N_2-saturated 0.1 M KOH were first tested (**Figure 3d**). For the activated Bi_2Te_3 NPs/C, the current density in N_2-saturated electrolyte was higher than that in the Ar-saturated one from -0.3 V_{RHE} to -0.8 V_{RHE}, indicating that activated Bi_2Te_3 NPs/C had

potential response toward N_2RR. By contrast, the commercial Bi_2Te_3/C exhibited similar polarization curve in both Ar-saturated and N_2-saturated electrolytes, suggesting its low activity toward N_2RR. The potentiostatic tests were further conducted in N_2-saturated 0.1 M KOH solution at different potentials for 2 h (**Figure S12**). The FEs of NH_3 were calculated by the detection of different potential liquid products based on UV spectrophotometer. As shown in **Figure 3e**, the FE_{NH3} for the activated Bi_2Te_3 NPs/C was higher than that of the commercial Bi_2Te_3/C at all applied potentials. Remarkably, the FE_{NH3} for activated Bi_2Te_3 NPs/C reached 7.9% at -0.4 V_{RHE}, which was 1.82-fold higher than that of the commercial Bi_2Te_3/C (4.3%). The FE_{NH3} for the activated Bi_2Te_3 NPs/C was higher than many non-noble metals-based catalysts and even outperformed several typical noble-metal catalysts, such as Au nanorods[22] (**Table S3**). Moreover, the yield rates for NH_3 of the different catalysts were further investigated. As shown in **Figure 3f**, the rate increased as the negative potential increased until -0.4 V_{RHE}, where an average value of NH_3 is 3.9 μg_{NH3} h^{-1} cm^{-2}. As the potential reached below -0.4 V_{RHE}, the hydrogen evolution reaction becomes the major reaction, as revealed by the polarization curve shown in **Figure 3d**. In control experiments (**Figure S13**), when N_2 was replaced by Ar, while keeping other reaction parameters unchanged, NH_3 could not be identified in the electrolyte. The same was observed when the activated Bi_2Te_3 NPs/C was replaced by a carbon paper or carbon. These control experiments confirmed that NH_3 was produced from the N_2RR catalyzed by the activated Bi_2Te_3 NPs/C. To corroborate the origin of the NH_3 generated from N_2RR, we designed isotopic labelling study using $^{15}N_2$ as the feeding gases.[42,43] The obtained $^{15}NH_4^+$ and $^{14}NH_4^+$ were measured by ^{1}H NMR spectroscopy of the reaction solution. The ^{1}H NMR spectra of the standards and the yielded $^{14}NH_4^+$ and $^{15}NH_4^+$ were shown in **Figure S14**. The isotopic labelled sample exhibited doublets, which correspond to $^{15}NH_4^+$. When using pure $^{14}N_2$ as a reference, triplets corresponding to $^{14}NH_4^+$ can be found. Those results confirm that the yielded NH_3 resulted from the activated Bi_2Te_3 NPs/C catalyzed N_2RR. Finally, the durability of the activated

Bi_2Te_3 NPs/C was tested by scanning at a constant potential of -0.4 V_{RHE} for 10 h (**Figure S15**), where the activated Bi_2Te_3 NPs/C maintained almost the same FE_{NH3} as the initial value.

To understand the intrinsic reason for the high performance of the Bi_2Te_3 NPs/C towards small molecules electroreduction, the Bi_2Te_3 NPs/C at the different stages during the catalytic process were characterized in detail. Before the electroreduction, the Bi_2Te_3 NPs/C was activated by cycling in 0.1 M KOH for 500 cycles. We can see that the activated Bi_2Te_3 NPs/C are porous structure (**Figure 4a**) with partial dissolution of Te (**Figure 4b**). The atomic ratio of Bi/Te changed from 40.6/59.4 into 62.3/37.7, as revealed by SEM-EDS, which was in lined with the ICP-AES results (**Table S4**). In addition, the EDS mappings showed that Bi and Te still distributed on the NPs uniformly (**Figure 4c**). HRTEM image revealed that the lattices were discontinuous in the activated Bi_2Te_3 NPs/C (**Figure 4d**). Therefore, the atomic arrangement of the activated Bi_2Te_3 NPs/C showed obvious structure change at the surface, which would affect the catalytic performance.[44,45] In addition, the discontinuous lattice formed by the obvious Te dissolution could lead to the formation of Te vacancies. The Bi 4f and Te 3d spectra of the activated Bi_2Te_3 NPs/C showed that both the surface Bi and surface Te were in the oxidation state, as revealed by X-ray photoelectron spectroscopy (**Figure S16**).

The activated Bi_2Te_3 NPs/C after ORR durability test was also investigated in detail. As shown in **Figure S17a**, they could still be well-dispersed on the carbon support, and the atomic ratio of Bi/Te could be largely maintained (69.5/30.5) (**Figure 4b**). Discontinuous lattices could also be observed here (**Figure S17b**). Furthermore, both Bi and Te still distributed on the NPs uniformly (**Figure S17c**). Based on the above experimental results, we further summarized the schematic diagram of the morphology and structural evolution of the Bi_2Te_3 NPs/C during ORR in **Figure 4e**. After electrochemical activation, the NPs changed to be a porous structure due to the partial dissolution of Te. As the reaction proceeds, the NPs maintained a porous hexagonal NP structure after the durability test, except that the degree of

porosity increases slightly with the further minor dissolution of Te. Above all, after the ORR durability test, the activated Bi_2Te_3 NPs/C could largely maintain their structure and composition, showing excellent ORR durability. As for CO_2RR and N_2RR, the activated Bi_2Te_3 NPs/C also exhibited good durability (**Figure S18-19**) with negligible changes in selectivity, composition, morphology and structure. In addition, the performances of the Bi_2Te_3 and commercial Bi_2Te_3 for ORR, CO_2RR and N_2RR have been included (**Figure S20-22**). As we can see, if the materials were not loaded on the carbon, their performances for the electrochemical reduction reactions are much worse.

Especially, Te vacancies formed after the Te dissolution form the Bi_2Te_3 NPs/C during the activation process may play a key role in the reduction reaction. To further confirm that the Te vacancies promote the activities of small molecules reduction in experiment, we compared the performances for ORR, CO_2RR and N_2RR of the Bi_2Te_3 NPs/C before and after electrochemical activation. We can see that the Bi_2Te_3 NPs/C without electrochemical activation exhibits much worse performances (**Figure S23-24**), clearly showing the important role of Te vacancies in the small molecules reduction reaction.

The DFT calculations have been carried out for the insightful understanding of such reduction active materials. To clearly observe the evident effect brought by the surface defect, the electronic distribution of bonding and anti-bonding near the Fermi level (E_F) between the pristine Bi_2Te_3 and defective Bi_2Te_3 with vacancy Te (V_{Te}) is presented. For the pristine Bi_2Te_3, the electronic distribution shows the coupling between the HOMO and LUMO. However, when the surface Te vacancy is introduced to the lattice, the charge density distribution of bonding and antibonding orbitals has obviously turned from delocalized to localized (**Figure 5a-5b**). The formation of the surface defect will significantly reconstruct the surface electronic distribution to activate the electroactivity for molecule reduction. To gain more insight into the origin of the electroactivity, we further interpret the electronic

properties given by different regions of Bi_2Te_3. With the introduction of surface Te vacancy, the Bi-6p has been significantly activated when compared to the pristine Bi_2Te_3. The Bi-6p bands has been boosted up with 0.87 eV towards the Fermi level, confirming the overall enhanced electroactivity (**Figure 5c**). From the deep layer to the surface of Bi_2Te_3, the evolution of the projected partial density of states (PDOS) of Te displays a gradual migration to the higher position close to E_F (**Figure 5d**). The surface Te has been activated from E_F -1.25 eV to E_F -0.25 eV with a positive 1.00 eV band offset, which is consistent with the electronic distribution change with V_{Te}. Simultaneously, the similar activation of Bi is also noted, in which the dominant Bi-6p bands have been boosted from E_F -1.75 eV to E_F -3.25 eV with a positive 1.25 eV band offset (**Figure 5e**). The Bi-bands locates at a lower position than Te-bands supports an electron-rich character. The migration of p-bands of surface metal to the E_F imply an oxidation state that is in a good agreement with the XPS results. Thus, the surface defect V_{Te} has largely promoted the reduction ability of Bi_2Te_3 based on the excitation of surface electron-rich Bi and electron-depletion channel Te to reach the optimal electronic environment for reduction reactions.

The optimal adsorption of key reactants, products and intermediates of ORR, CO_2RR and N_2RR are shown in **Figure 5f-h**. The summary of the adsorption energies and bond length is supplied in **Table S5**. The active bonding between the surface and adsorbates with only slight distortion on the local Bi_2Te_3 structure demonstrates a smooth and stable reduction process depends on the electroactive surface, which confirms the good durability tests. We further analyze the universal reduction reactivity of Bi_2Te_3 from an energetic perspective regarding the free energy of the reaction pathway of ORR, N_2RR in alkaline condition and CO_2RR in acidic condition. To achieve high selectivity of H_2O_2 with 2-electron transfer rather than the conventional 4-electron ORR, the determining step by the formation of the key intermediate [OOH]* become pivotal (**Figure 5i**). Notably, [OOH]* shows much stronger

downhill towards the formation of $[H_2O_2]$* rather than the dissociation of O-H bonding. The further adsorption of the proton from water dissociation to form $[H_2O_2]$* exhibits a significant drop that is nearly 2 eV larger than the formation of [O]*, which is in a good agreement with the ultra-high selectivity of H_2O_2 during the operation range. Furthermore, the spontaneous desorption of H_2O_2 will ensure efficient 2-electron ORR. Further investigation of CO_2RR also reflects an energetically preferred reaction with total reaction releases heat of 0.35 eV. (**Figure 5j**). The first adsorption of the proton is prone to the formation of [HCOO]* rather than [COOH]*. The formation of [COOH]* will confront an energy barrier of 0.27 eV that leads to a lower CO_2RR efficiency when compared with the route of [HCOO]*. The transition barrier of the CO_2RR is 0.17 and 0.31 eV, respectively. The continuous downhill physiochemical trend of CO_2RR supports a good reactivity while the appropriate adsorption energy of HCOOH will also ensure a good efficiency. For the N_2RR process, the first protonation process of the N_2 molecule is usually considered as the determining step for the N_2RR.[46] For the surface defective Bi_2Te_3, the key energy barrier is 0.36 V at zero electrode potential (U = 0 V) (**Figure 5k**). When U= -0.36 V is applied, the whole N_2RR becomes spontaneous, which is closer to the polarization curve test. As an important indicator to evaluate the N_2RR performance, we calculate the overpotential η according to U(equilibrium) - U(rate-limiting), where the U(equilibrium) is around about -0.16 V for the reaction N_2RR. Thus, the overpotential of N_2RR on Bi_2Te_3 will be (-0.16) - (-0.36) = 0.2 V, which is lower than some previously well-studied systems such as Ru and Re,[47] indicating the great electroactivity towards N_2RR of the surface defective Bi_2Te_3. Therefore, both the electronic and energetic analysis demonstrates the great electroactivity towards the reduction reactions. The defect-induced optimized surface electronic environment endows Bi_2Te_3 great potential as a promising multi-functional electrocatalyst for facile synthesis of highly valuable small molecules for broad applications in industrials.

In conclusion, we first demonstrated that ultrathin Bi_2Te_3 NPs can be adopted as highly universal and robust electrocatalysts for the reduction of small molecules (O_2, CO_2 and N_2). When the activated Bi_2Te_3 NPs/C was evaluated as the ORR electrocatalyst in 0.1 M KOH, it exhibited excellent ORR selectivity toward H_2O_2 production with almost 100% selectivity between 0.2 V_{RHE} and 0.6 V_{RHE}. When the activated Bi_2Te_3 NPs/C was adopted as CO_2RR electrocatalyst in 0.5 M $NaHCO_3$, it enabled superior activity with large HCOOH partial current density of 24.2 mA cm^{-2} at -1.1 V_{RHE}, as well as excellent selectivity with FE_{HCOOH} of 89.6%. As for the N_2RR, the activated Bi_2Te_3 NPs/C had been demonstrated to serve as a highly efficient electrocatalyst for N_2RR with the FE_{NH3} of 7.9% for at -0.4 V_{RHE} in 0.1 M KOH. They also showed enhanced durability after a long period of electrolysis for all the three electrocatalytic reactions. Detailed characterizations revealed that, after electrochemical activation, an obvious Te dissolution happened on the Bi_2Te_3 NPs, which creates a large amount of Te vacancies in the activated Bi_2Te_3 NPs. Theoretical calculations confirmed that the formation of Te vacancy will completely modulate the surface of Bi_2Te_3 towards electroactive and reductive feature as the active sites for the universal for the high-valued small molecules via energetically favorbale pathways. This work not only showed that the activated Bi_2Te_3 NPs/C are universal catalysts for the electroreduction of small molecules, but also provided a powerful material foundation for potential electrocatalysis.

Supporting Information
Supporting Information is available from the Wiley Online Library or from the author.

Acknowledgements
This work was financially supported by the Ministry of Science and Technology (2016YFA0204100, 2017YFA0208200), the National Natural Science Foundation of China (21571135), Young Thousand Talented Program, Natural Science Foundation of Jiangsu Higher Education Institutions (17KJB150032), the project of scientific and technologic infrastructure of Suzhou (SZS201708), the Priority Academic Program Development of Jiangsu Higher Education Institutions (PAPD), and the start-up supports from Soochow University. Nan Zhang, Fangfang Zheng and Bolong Huang contributed equally to this work.

Received: ((will be filled in by the editorial staff))
Revised: ((will be filled in by the editorial staff))
Published online: ((will be filled in by the editorial staff))

[1]. Z. Lu, G. Chen, S. Siahrostami, Z. Chen, K. Liu, J. Xie, L. Liao, T. Wu, D. Lin, Y. Liu, T. F. Jaramillo, J. K. Nørskov, Y. Cui, *Nat. Catal.* **2018**, *1*, 156.

[2]. Y. Jiang, P. Ni, C. Chen, Y. Lu, P. Yang, B. Kong, A. Fisher, X. Wang, *Adv. Energy Mater.* **2018**, *8*, 1801909.

[3]. Y. P. Zhu, C. Guo, Y. Zheng, S. Z. Qiao, *Acc. Chem. Res.* **2017**, *50*, 915.

[4]. N. Han, Y. Wang, L. Ma, J. Wen, J. Li, H. Zheng, K. Nie, X. Wang, F. Zhao, Y. Li, J. Fan, J. Zhong, T. Wu, D. J. Miller, J. Lu, S. T. Lee, Y. Li, *Chem* **2017**, *3*, 652.

[5]. Z. Weng, J. Jiang, Y. Wu, Z. Wu, X. Guo, K. L. Materna, W. Liu, V. S. Batista, G. W. Brudvig, H. Wang, *J. Am. Chem. Soc.* **2016**, *138*, 8076.

[6]. J. G. Chen, R. M. Crooks, L. C. Seefeldt, K. L. Bren, R. M. Bullock, M. Y. Darensbourg, P. L. Holland, B. Hoffman, M. J. Janik, A. K. Jones, M. G. Kanatzidis, P. King, K. M. Lancaster, S. V. Lymar, P. Pfromm, W. F. Schneider, R. R. Schrock, *Science* **2018**, *360*, aar6611.

[7] L. He, X. Sun, H. Zhang, F. Shao, *Angew. Chem. Int. Ed.* **2018**, *57*, 12453.

[8]. W. Qiu, X. Y. Xie, J. Qiu, W. H. Fang, R. Liang, X. Ren, X. Ji, G. Cui, A. M. Asiri, G. Cui, B. Tang, X. Sun, *Nat. Commun.* **2018**, *9*, 3485.

[9]. D. Iglesias, A. Giuliani, M. Melchionna, S. Marchesan, A. Criado, L. Nasi, M. Bevilacqua, C. Tavagnacco, F. Vizza, M. Prato, P. Fornasiero, *Chem* **2018**, *4*, 106.

[10]. T. P. Fellinger, F. Hasché, P. Strasser, *J. Am. Chem. Soc.* **2012**, *134*, 4072.

[11]. J. S. Jirkovský, I. Panas, E. Ahlberg, M. Halasa, S. Romani, D. J. Schiffrin, *J. Am. Chem. Soc.* **2011**, *133*, 19432.

[12]. H. W. Kim, M. B. Ross, N. Kornienko, L. Zhang, J. Guo, P. Yang, B. D. McCloskey, *Nat. Catal.* **2018**, *1*, 282.

[13]. C. Liu, B. C. Colón, M. Ziesack, P. A. Silver, D. G. Nocera, *Science* **2016**, *352*, 1210.

[14]. M. Schreier, F. Héroguel, L. Steier, S. Ahmad, J. S. Luterbacher, M. T. Mayer, J. Luo, M. Grätzel, *Nat. Energy* **2017**, *2*, 17087.

[15]. S. Enthaler, J. von Langermann, T. Schmidt, *Energy Environ. Sci.* **2010**, *3*, 1207.

[16]. K. Jiang, H. Wang, W. B. Cai, H. Wang, *ACS Nano* **2017**, *11*, 6451.

[17]. J. Wu, Y. Huang, W. Ye, Y. Li, *Adv. Sci.* **2017**, *4*, 1700194.

[18]. L. Zhang, Z. J. Zhao, J. Gong, *Angew. Chem. Int. Ed.* **2017**, *56*, 11326.

[19]. D. D. Zhu, J. L. Liu, S. Z. Qiao, *Adv. Mater.* **2016**, *28*, 3423.

[20] A. Vasileff, C. Xu, Y. Jiao, Y. Zheng, S. Z. Qiao, *Chem* **2018**, *4*, 1809.

[21]. Z. Geng, X. Kong, W. Chen, H. Su, Y. Liu, F. Cai, G. Wang, J. Zeng, *Angew. Chem. Int. Ed.* **2018**, *57*, 6054.

[22]. D. Bao, Q. Zhang, F. L. Meng, H. X. Zhong, M. M. Shi, Y. Zhang, J. M. Yan, Q. Jiang, X. B. Zhang, *Adv. Mater.* **2017**, *29*, 1604799.

[23]. S. Licht, B. Cui, B. Wang, F. F. Li, J. Lau, S. Liu, *Science* **2014**, *345*, 637.

[24]. H. Daims, E. V. Lebedeva, P. Pjevac, P. Han, C. Herbold, M. Albertsen, N. Jehmlich, M. Palatinszky, J. Vierheilig, A. Bulaev, R. H. Kirkegaard, M. von Bergen, T. Rattei, B. Bendinger, P. H. Nielsen, M. Wagner, *Nature* **2015**, *528*, 504.

[25]. C. Guo, J. Ran, A. Vasileff, S. Z. Qiao, *Energy Environ. Sci.* **2018**, *11*, 45.

[26]. Z. Geng, Y. Liu, X. Kong, P. Li, K. Li, Z. Liu, J. Du, M. Shu, R. Si, J. Zeng, *Adv. Mater.* **2018**, *30*, 1803498.

[27]. S. J. Li, D. Bao, M. M. Shi, B. R. Wulan, J. M. Yan, Q. Jiang, *Adv. Mater.* **2017**, *29*, 1700001.

[28]. M. M. Shi, D. Bao, B. R. Wulan, Y. H. Li, Y. F. Zhang, J. M. Yan, Q. Jiang, *Adv. Mater.* **2017**, *29*, 1606550.

[29]. Y. Liu, Y. Su, X. Quan, X. Fan, S. Chen, H. Yu, H. Zhao, Y. Zhang, J. Zhao, *ACS Catal.* **2018**, *8*, 1186.

[30]. J. Han, X. Ji, X. Ren, G. Cui, L. Li, F. Xie, H. Wang, B. Li, X. Sun, *J. Mater. Chem. A* **2018**, *6*, 12974.

[31]. S. Chen, S. Perathoner, C. Ampelli, C. Mebrahtu, D. Su, G. Centi, *Angew. Chem. Int. Ed.* **2017**, *56*, 2699.

[32]. L. Zhang, X. Ji, X. Ren, Y. Ma, X. Shi, Z. Tian, A. M. Asiri, L. Chen, B. Tang, X. Sun, *Adv. Mater.* **2018**, *30*, 1800191.

[33]. A. Zhang, R. He, H. Li, Y. Chen, T. Kong, K. Li, H. Ju, J. Zhu, W. Zhu, J. Zeng, *Angew. Chem. Int. Ed.* **2018**, *57*, 10954.

[34]. Y. Jia, L. Zhang, G. Gao, H. Chen, B. Wang, J. Zhou, M. T. Soo, M. Hong, X. Yan, G. Qian, J. Zou, A. Du, X. Yao, *Adv. Mater.* **2017**, *29*, 1700017.

[35]. S. Chen, Z. Chen, S. Siahrostami, D. Higgins, D. Nordlund, D. Sokaras, T. R. Kim, Y. Liu, X. Yan, E. Nilsson, R. Sinclair, J. K. Nørskov, T. F. Jaramillo, Z. Bao, *J. Am. Chem. Soc.* **2018**, *140*, 7851.

[36]. S. Siahrostami, A. Verdaguer-Casadevall, M. Karamad, D. Deiana, P. Malacrida, B. Wickman, M. Escudero-Escribano, E. A. Paoli, R. Frydendal, T. W. Hansen, I. Chorkendorff, I. E. L. Stephens, J. Rossmeisl, *Nat. Mater.* **2013**, *12*, 1137.

[37]. A. Verdaguer-Casadevall, D. Deiana, M. Karamad, S. Siahrostami, P. Malacrida, T. W. Hansen, J. Rossmeisl, I. Chorkendorff, I. E. L. Stephens, *Nano Lett.* **2014**, *14*, 1603.

[38]. Z. Zheng, Y. H. Ng, D. W. Wang, R. Amal, *Adv. Mater.* **2016**, *28*, 9949.

[39]. Y. C. Ha, H. J. Sohn, G. J. Jeong, C. K. Lee, K. I. Rhee, *J. Applied. Electrochem.* **2000**, *30*, 315.

[40]. N. Han, Y. Wang, H. Yang, J. Deng, J. Wu, Y. Li, Y. Li, *Nat. Commun.* **2018**, *9*, 1320.

[41]. S. Gao, Y. Lin, X. Jiao, Y. Sun, Q. Luo, W. Zhang, D. Li, J. Yang, Y. Xie, *Nature* **2016**, *529*, 68.

[42]. Y. Liu, M. Han, Q. Xiong, S. Zhang, C. Zhao, W. Gong, G. Wang, H. Zhang, H. Zhao, *Adv. Energy Mater.* **2019**, *9*, 1803935.

[43]. M. Wang, S. Liu, T. Qian, J. Liu, J. Zhou, H. Ji, J. Xiong, J. Zhong, C. Yan, *Nat. Commun.* **2019**, *10*, 341.

[44]. X. Zhao, L. Zhou, W. Zhang, C. Hu, L. Dai, L. Ren, B. Wu, G. Fu, N. Zheng, *Chem* **2018**, *4*, 1080.

[45]. P. Liu, R. Qin, G. Fu, N. Zheng, *J. Am. Chem. Soc.* **2017**, *139*, 2122.

[46]. J. Zhao, Z. Chen, *J. Am. Chem. Soc.* **2017**, *139*, 12480.

[47]. J. H. Montoya, C. Tsai, A. Vojvodic, J. K. Nørskov, *ChemSusChem* **2015**, *8*, 2180.

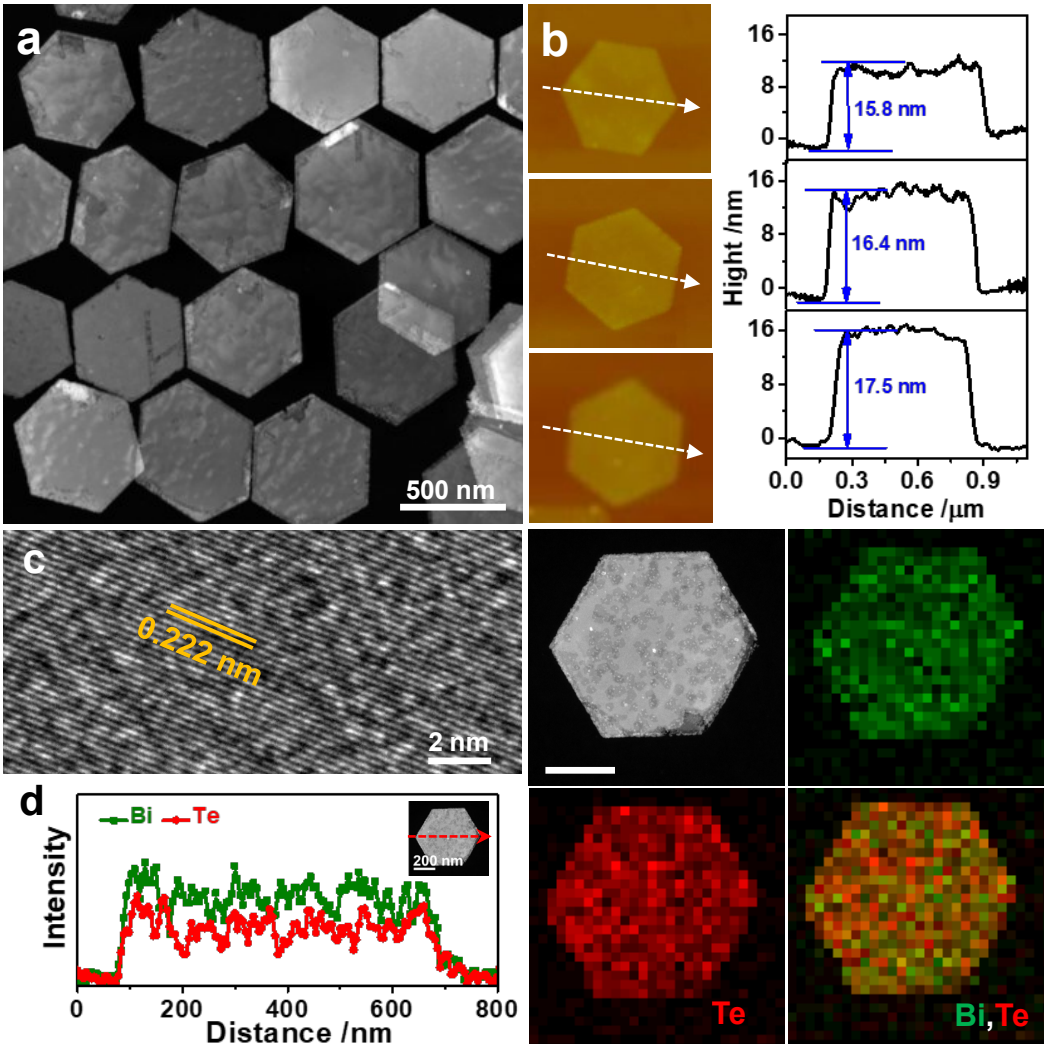

Figure 1. (a) HAADF-STEM image, (b) AFM images of the Bi_2Te_3 NPs. (c) HRTEM image, (d) line scan analysis, and (e) HAADF-STEM image and STEM-EDS elemental mappings of a Bi_2Te_3 NP.

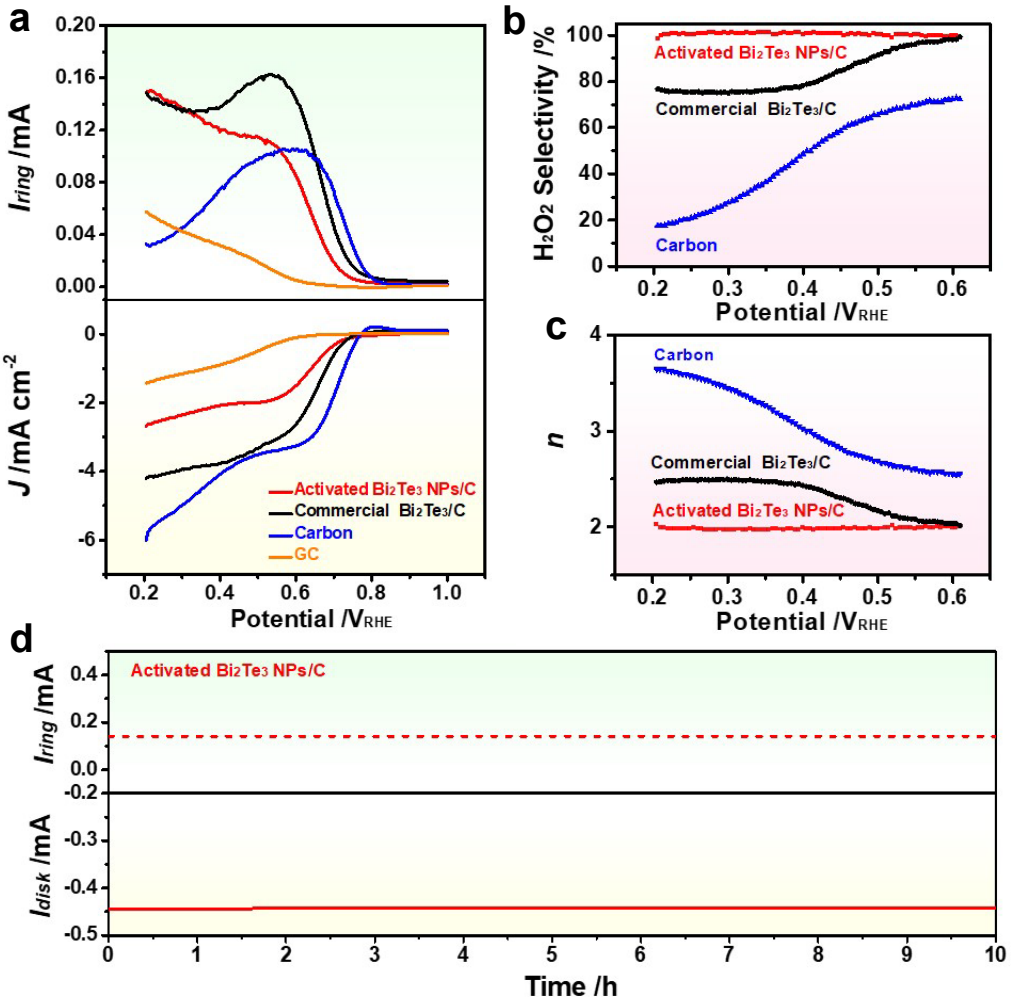

Figure 2. (a) RRDE voltammograms of the activated Bi_2Te_3 NPs/C, commercial Bi_2Te_3/C, carbon, and GC at 1600 rpm in O_2-saturated 0.1 M KOH with the disk current density and ring current. The scan rate is 10 mV/s. (b) H_2O_2 selectivity as a function of the applied potential. (c) The calculated values of n as a function of the applied potential. (d) 10 h durability test for the activated Bi_2Te_3 NPs/C at 0.4 V_{RHE} for disk and 1.2 V_{RHE} for ring.

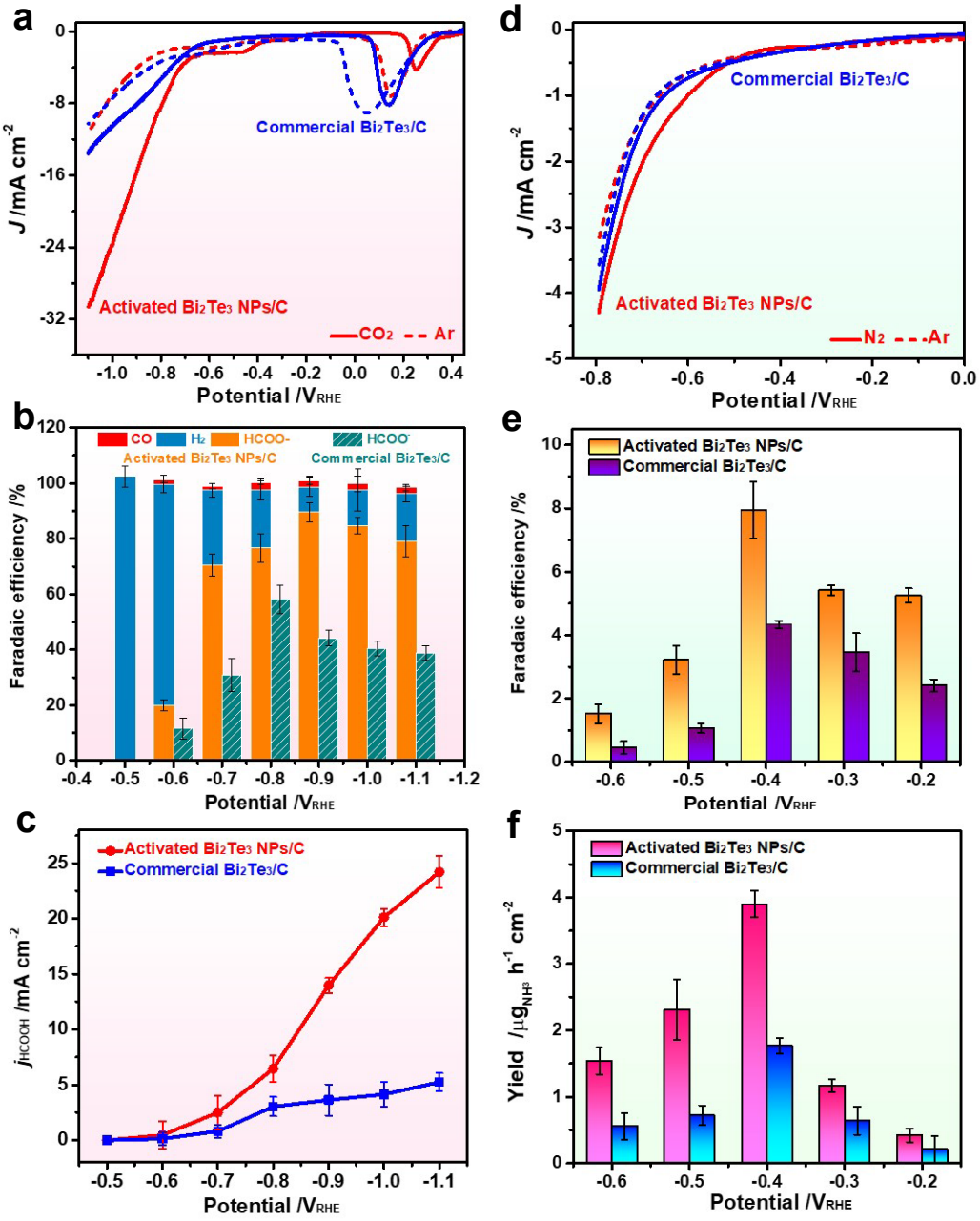

Figure 3. (a) Polarization curves of the activated Bi_2Te_3 NPs/C and commercial Bi_2Te_3/C in Ar- and CO_2-saturated 0.5 M $NaHCO_3$. (b) Potential-dependent FEs of HCOOH, CO, H_2 for activated Bi_2Te_3 NPs/C and FE_{HCOOH} for commercial Bi_2Te_3/C (dashed blue line). (c) Potential-dependent HCOOH partial current density of the activated Bi_2Te_3 NPs/C and commercial Bi_2Te_3/C. (d) Polarization curves of the two catalysts in Ar- and N_2-saturated 0.1 M KOH. Potential-dependent (e) FE_{NH3} and (f) yield rate of NH_3 production for the activated Bi_2Te_3 NPs/C and commercial Bi_2Te_3/C.

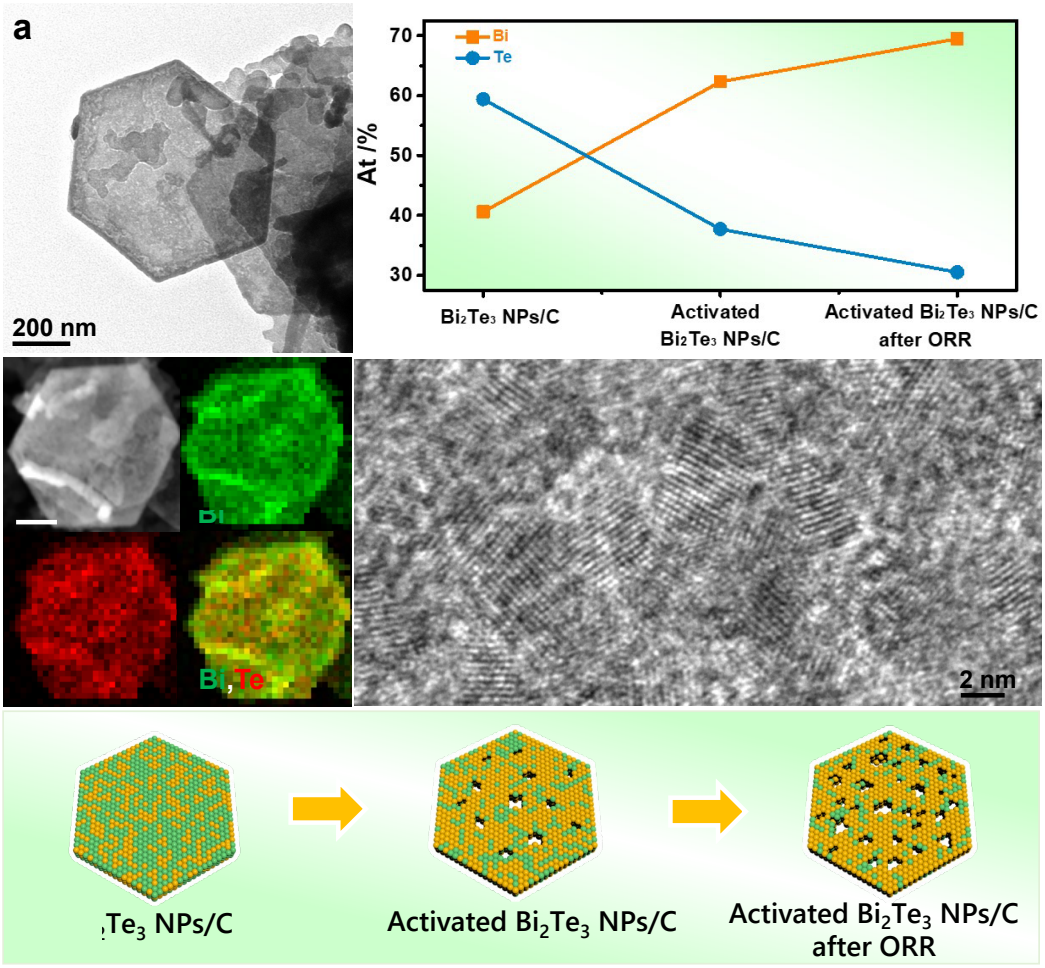

Figure 4. (a) TEM image, (b) composition changes of Bi and Te of the Bi_2Te_3 NPs/C during ORR based on SEM-EDS, (c) STEM image and EDS mappings, and (d) HRTEM image of the activated Bi_2Te_3 NPs/C. (e) Schematic illustration of morphology and structural evolution of the Bi_2Te_3 NPs/C during ORR.

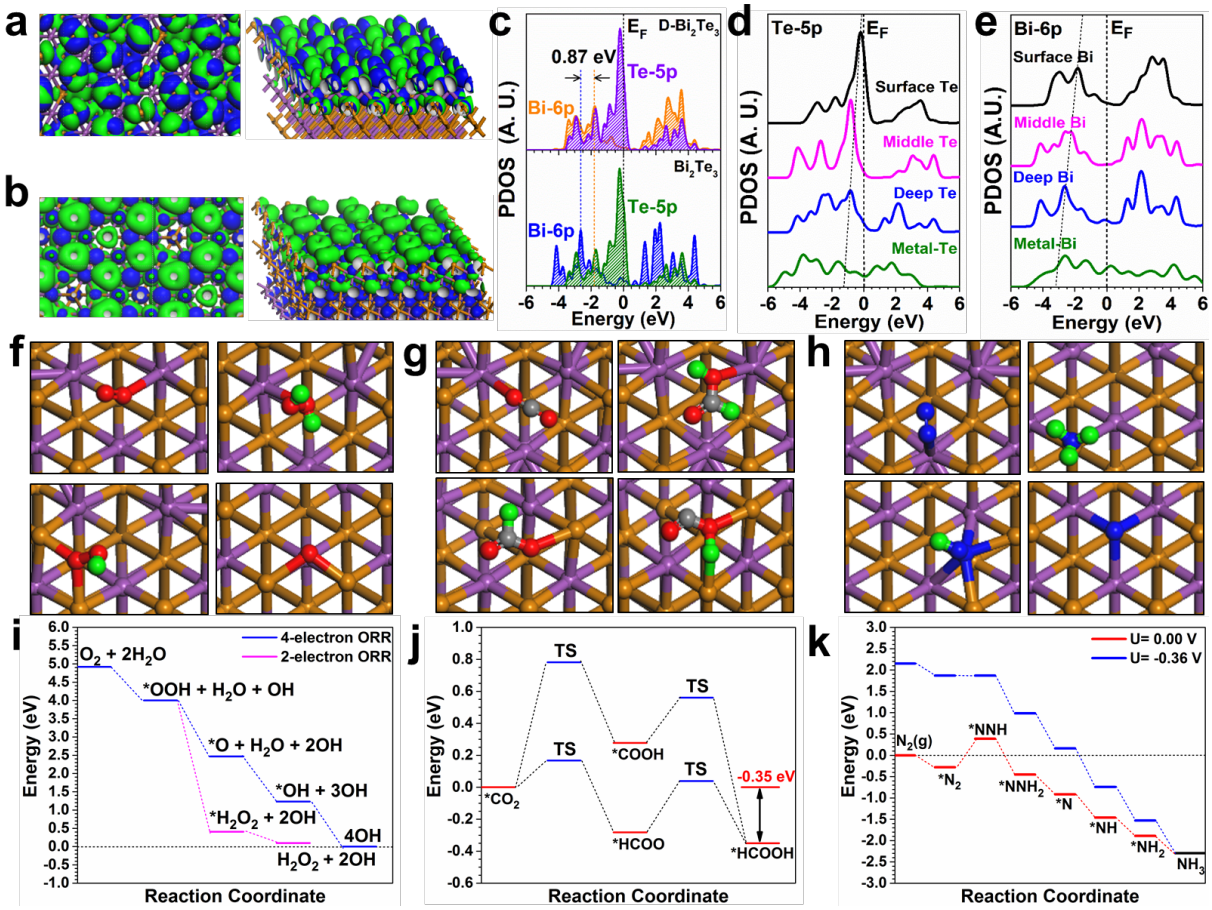

Figure 5. (a) The electronic orbital distribution of pristine Bi_2Te_3. Green Isosurface = HOMO, Blue Isosurface = LUMO. (b) The electronic orbital distribution of surface defective Bi_2Te_3. Green Isosurface = HOMO, Blue Isosurface = LUMO. (c) The comparison of PDOSs between pristine Bi_2Te_3 and surface defective Bi_2Te_3 (D-Bi_2Te_3). (d) The site-dependent PDOSs of Te from surface regions towards metal Te. (e) The site-dependent PDOSs of Bi from surface regions towards metal Bi. (f) The local structural configurations for adsorption of O_2, H_2O_2, [OOH]* and [O]* in ORR. (g) The local structural configurations for adsorption of CO_2, HCOOH, [HCOO]* and [COOH]* in CO_2RR. (h) The local structural configurations for adsorption of N_2, NH_3, [NNH]* and [N]* in N_2RR. Red Balls = O, Green Balls= H, Blue Balls = N, Grey Balls = C, Brown Balls = Te and Purple Balls = Bi. (i) Free energy pathways for ORR under the alkaline condition. (j) Free energy pathways for CO_2RR under the acidic condition. (k) Free energy pathways for N_2RR under the alkaline condition.

The table of contents entry

The ultrathin activated Bi_2Te_3 nanoplates (NPs) have been demonstrated as highly universal and robust electrocatalysts for the electroreduction of small molecules (O_2, CO_2 and N_2), where they exhibit nearly 100% H_2O_2 selectivity for ORR, 89.6% Faradaic efficiency (FE) of HCOOH for CO_2RR and 7.9% FE of NH_3 for N_2RR, as well as enhanced durability, showing a new class of robust electrocatalysts for small molecules conversion with potential practical applications.

Keyword: Bi_2Te_3 nanoplate • Universality • Oxygen reduction reaction • Carbon dioxide reduction reaction • Nitrogen reduction reaction

Exploring Bi_2Te_3 nanoplates as versatile catalysts for electrochemical reduction of small molecules

Nan Zhang[+], Fangfang Zheng[+], Bolong Huang[+], Yujin Ji, Qi Shao, Youyong Li, Xiangheng Xiao, Xiaoqing Huang[*]

ToC figure